THE JOURNAL OF BIOLOGICAL CHEMISTRY VOL. 290, NO. 36, pp. 22127–22142, September 4, 2015

Fibroblast Growth Factor 9 Imparts Hierarchy and Vasoreactivity to the Microcirculation of Renal Tumors and Suppresses Metastases*[S]

Received for publication, March 16, 2015, and in revised form, July 14, 2015 Published, JBC Papers in Press, July 16, 2015, DOI 10.1074/jbc.M115.652222

Hao Yin[‡1,2], **Matthew J. Frontini**[‡§1], **John-Michael Arpino**[‡¶], **Zengxuan Nong**[‡], **Caroline O'Neil**[‡], **Yiwen Xu**[‡¶], **Brittany Balint**[‡¶], **Aaron D. Ward**[¶], **Subrata Chakrabarti**[‖], **Christopher G. Ellis**[¶], **Robert Gros**[‡**‡‡3], **and J. Geoffrey Pickering**[‡§¶‡‡ §§4]

From the [‡]*Robarts Research Institute and Departments of* [§]*Biochemistry,* [¶]*Medical Biophysics,* [‖]*Pathology,* [**]*Physiology and Pharmacology, and* [‡‡]*Medicine, University of Western Ontario,* [§§]*London Health Sciences Centre, London, Ontario N6A 5A5, Canada*

Background: Tumor microvessels are non-hierarchical and regulate blood flow poorly.
Results: Delivery of fibroblast growth factor 9 (FGF9) reconfigured the chaotic renal tumor vasculature into a fortified, hierarchical, and vasoreactive network by activating PDGFRβ^+-stromal cells. Tumor hypoxia and metastases declined.
Conclusion: FGF9 can generate a vasoreactive tumor microcirculation.
Significance: This advanced state of microvascular differentiation could favorably impact tumor behavior.

Tumor vessel normalization has been proposed as a therapeutic paradigm. However, normal microvessels are hierarchical and vasoreactive with single file transit of red blood cells through capillaries. Such a network has not been identified in malignant tumors. We tested whether the chaotic tumor microcirculation could be reconfigured by the mesenchyme-selective growth factor, FGF9. Delivery of FGF9 to renal tumors in mice yielded microvessels that were covered by pericytes, smooth muscle cells, and a collagen-fortified basement membrane. This was associated with reduced pulmonary metastases. Intravital microvascular imaging revealed a haphazard web of channels in control tumors but a network of arterioles, bona fide capillaries, and venules in FGF9-expressing tumors. Moreover, whereas vasoreactivity was absent in control tumors, arterioles in FGF9-expressing tumors could constrict and dilate in response to adrenergic and nitric oxide releasing agents, respectively. These changes were accompanied by reduced hypoxia in the tumor core and reduced expression of the angiogenic factor VEGF-A. FGF9 was found to selectively amplify a population of PDGFRβ-positive stromal cells in the tumor and blocking PDGFRβ prevented microvascular differentiation by FGF9 and also worsened metastases. We conclude that harnessing local mesenchymal stromal cells with FGF9 can differentiate the tumor microvasculature to an extent not observed previously.

Solid tumors recruit a vascular network to sustain their growth. This vascular response underlies the rationale for the use of anti-angiogenic agents for cancer therapy (1, 2). However, despite an appealing premise and some clinical success, anti-angiogenic therapy has not transformed cancer management. As monotherapy, anti-angiogenic drugs have been effective for relatively few tumors (3). When combined with other anti-tumor drugs the impact has been broader, but gains in progression-free survival remain modest (3).

The less than anticipated advances with anti-angiogenesis approaches suggest that the relationship between tumor vessels and tumor behavior is more complex than originally considered (3, 4). Important in this regard is that vessels within tumors bear little resemblance to those in healthy tissues. Tumor vessels are dilated, their walls can be sparsely populated by pericytes or vascular smooth muscle cells (SMCs),[5] and branching is haphazard (5, 6). These abnormalities, by virtue of the attendant perfusion anomalies, can impair chemotherapeutic drug delivery and blunt the response to radiation therapy (4, 7). Moreover, unresolved hypoxia can enhance tumor invasiveness (8). It has also been found that, by further exacerbating hypoxia, anti-angiogenic therapy can worsen the metastatic phenotype (9, 10).

With these limitations in mind, an alternative approach to targeting the tumor vasculature has been proposed, based not on obliterating tumor vessels but on normalizing them. Several studies have demonstrated that tumor vessels have the capacity to improve their integrity (11–13). This includes structural improvements in response to anti-vascular endothelial growth factor (VEGF) agents, which can prune the otherwise chaotic tumor vasculature (11).

However, shifting the therapeutic paradigm from ablating to normalizing tumor vessels demands knowing the extent to which microvessels within the tumor environment can truly

* This work was supported in part by Canadian Cancer Society Grant 701080, Canadian Institutes of Health Research Grants FRN-11715 and FRN-126148, Heart and Stroke Foundation of Canada (HSFC) Grant T7081, and the University of Western Ontario (POEM). J. G. P., M. J. F., and Z. N. hold a patent relating to FGF9 and vascular remodeling, assigned to the University of Western Ontario.
[S] This article contains supplemental Videos S1–S5.
[1] Both authors contributed equally to this article.
[2] Supported by a Canadian Institutes of Health Research Fellowship.
[3] Supported by a New Investigator Award HSFC.
[4] Holds the Heart and Stroke Foundation of Ontario/Barnett-Ivey Chair. To whom correspondence should be addressed: London Health Sciences Centre, 339 Windermere Rd., London, Ontario, Canada N6A 5A5. Tel.: 519-663-3973; Fax: 519-434-3278; E-mail: gpickering@robarts.ca.

[5] The abbreviations used are: SMC, smooth muscle cells; SNP, sodium nitroprusside.

normalize. There are a number of critical features of a normal microvasculature that remain elusive in tumors. One such feature is the structured hierarchy of arterioles, capillaries, and venules. This is largely missing in the tumor vasculature, which instead is characterized by disordered loops and meshworks (11, 14, 15). As well, the caliber of the channels in tumors is notably wider than that of normal capillaries, even after pruning by anti-VEGF agents (11, 15, 16). Furthermore, the phenomenon of single file red blood cell flow through capillaries, fundamental to efficient gas and nutrient exchange, has not been found in tumors. Finally, the ability to locally regulate perfusion through vasoreactivity is a major distinction. Although growing tumors can surround and co-opt native arteries, the ability of neovessels within the tumor to respond to vasomotor signals has not been identified.

Fibroblast growth factor 9 (FGF9) is a mesenchyme-targeting growth factor necessary for embryonic development of the lung, heart, intestine, and cerebellum (17–20). FGF9 is noteworthy in the context of angiogenesis because, unlike other FGF family members, it has little, if any, direct effect on endothelial tube formation. Instead, FGF9 can promote the layering of mural cells around new blood vessels in ischemic muscle (21). Stimulating the mural compartment of blood vessels and not the endothelial cells is intriguing in the context of tumors, given the excessive drive for angiogenesis and abundance of poorly wrapped endothelial channels. However, whether FGF9 can modify this pathological vascularization process is not known.

Therefore, we have investigated if delivery of FGF9 can impact the tumor microvasculature. We report a striking maturation of the microcirculation, with hierarchy and vasoreactivity, via extra-endothelial, stromal cell activation.

Experimental Procedures

Cell Culture—Renca cells (ATCC, CRL-2947), a transformed kidney cell line from BALB/cCR mice, were maintained in RPMI 1640 (Invitrogen) containing 10% fetal bovine serum. Cultures of Renca cells expressing either GFP or human FGF9 were generated by infection with adenovirus expressing the respective cDNA for 16 h at 37 °C. Mouse dermal fibroblasts were harvested from the skin of C57BL/6 mice and studied at the 3–4th subculture. Mouse embryo fibroblasts were harvested and cultured as previously described (22). 10T1/2 cells were obtained from ATCC. Cell proliferation was assessed by harvesting cells at the designated times with trypsin and counting of trypan blue-excluding cells using a hemacytometer. Cells in triplicate wells were counted every other day over a period of 5 or 7 days. Recombinant human FGF9 was purchased from R&D Systems.

Orthotopic Renal Carcinoma Model—Female BALB/c mice (Charles River) at 2 months of age were used and all experiments were conducted in accordance with the University of Western Ontario Animal Use Subcommittee. Implantation of Renca cells in the subcapsular space of female BALB/c mice yields an orthotopic tumor model that mimics the behavior of adult human renal cell carcinoma, including spontaneous metastases to the lung (23). Orthotopic primary tumors were generated from 2.5×10^5 Renca cells resuspended in phosphate-buffered saline (PBS) and mixed 1:1 (v/v) with growth factor-reduced Matrigel (BD Biosciences). Cell-Matrigel suspensions were injected as 30-μl aliquots into the subcapsular space of the left kidney of BALB/c mice. On designated days, animals were euthanized with isofluorane inhalation and both kidneys harvested for histologic analyses. Renca cells were transduced with adenovirus encoding either GFP or human FGF9. Immunostaining the resulting tumors for CD4 and CD8 revealed minimal immune reaction and no difference between control and FGF9-expressing tumors (2.6 ± 0.6 *versus* 3.0 ± 0.3 for CD4, $p = 0.49$; 3.5 ± 0.5 *versus* 3.9 ± 0.7 for CD8, $p = 0.69$). Metastatic burden was quantified on the lung surface and in paraffin-embedded lung mid-zone cross-sections, 14 days after injection. For this, lungs were fixed by immersion in 10% neutral-buffered formalin or with intratracheal instillation of 4% paraformaldehyde followed by immersion fixation.

Immunoblotting—Cell and tissues lysates were separated by SDS-PAGE and protein expression was assessed by Western blot analysis with chemiluminescent detection. FGF9 was detected using a goat polyclonal antibody raised against human FGF9 (1:500, R&D Systems) and α-tubulin detected with a mouse monoclonal antibody (clone B-5-1-2; 1:20,000, Sigma).

Transcript Analysis by RT-PCR—RNA was extracted from Renca cells and whole tumors with TRIzol (Life Technologies) and RNeasy (Qiagen), subjected to reverse transcription, and the resulting cDNA amplified by PCR. To screen for FGFR expression, custom primers were designed (Primer3 software) and synthesized (Sigma) and amplification was undertaken with 26 cycles of 94 °C (30 s), 58 °C (1 min), and 72 °C (1 min). Products were separated by electrophoresis and visualized by staining with SyberSafe (New England Biolabs) and UV illumination. To assess FGF9 transgene expression, quantitative RT-PCR was undertaken using TaqMan chemistry (TaqMan Gene Expression Assays, Hs00181829_m1, Life Technologies) and a ViiA 7 Real-time PCR System (Life Technologies). VEGF-A mRNA level was similarly quantified (Mm01281449_m1, Life Technologies). Gene expression was determined using the $\Delta\Delta C_t$ method and mouse 18S and Gapdh signals (Mm03928890_g1, Mm99999915_g1, Life Technologies). To screen for candidate gene expression changes within renal tumors, primers were synthesized (Sigma) for 20 genes using sequences listed in Table 1. Sequences were based on recommendations (OriGene Technologies, Rockville, MD), and quantitative real-time PCR was performed in triplicate using RT2 SYBR Green ROX PCR Mastermix (Qiagen) on ViiA 7 Real-time PCR System (Life Technologies) and $\Delta\Delta C_t$ analysis.

Histology and Immunostaining—Tumors were fixed for 16 h in 4% paraformaldehyde or for 8 h in Tris-buffered zinc and embedded in paraffin. Five-μm thick sections were stained with hematoxylin and eosin or were immunostained using biotinylated rat anti-mouse CD31 antibody (Clone MEC13.3, BD Biosciences), goat anti-VE-cadherin polyclonal antibody (AF1002, R&D Systems), mouse anti-smooth muscle α-actin antibody conjugated with alkaline phosphatase-conjugated (Clone 1A4, Sigma), rabbit anti-NG2 polyclonal antibody (AB5320, EMD Millipore), or rabbit anti-Ki-67 monoclonal antibody (ab16667, Abcam). Unconjugated primary antibodies were reacted with biotinylated donkey anti-rabbit IgG (711-065-152, Jackson

TABLE 1
Primer sequences used for polymerase chain reactions

Gene	Forward primer	Reverse primer
Fgfr1	ATCCTCGGAAGATGATGACG	GAAGGCACCACAGAATCCAT
Fgfr2 IIIb	AGGAGCACCGTACTGGACCAACA	GCAGACTGGTTGGCCTGCCC
Fgfr2 IIIc	GGATGGGGTGCACTTGGGGC	CGGCGGCCTTCAGGACCTTG
Fgfr3 IIIb	ATTTCATAGGCGTGGCTGAG	GACAAGGGGTGTGTTGGAGT
Fgfr3 IIIc	CCACCGACAAGGAGCTAGAG	TCGCATCATCTTTCAGCATC
Fgfr4	CTTCCTTCCTGAGGATGCTG	CTGTCCATCCTTGAGCCAGT
Actb	TGGGTCAGAAGGATTCCTATGT	TGTACGTTGCTATCCAGGCTG
Pdgfb	AATGCTGAGCGACCACTCCATC	TCGGGTCATGTTCAAGTCCAGC
Pdgfd	CTGTCAACTGGAAGTCCTGCAC	CCCTTCTCTTGAAATGTCCAGGC
Pdgfra	CTGGCTCGAAGTCAGATCCACA	GACTTGTCTCCAAGGCATCCTC
Pdgfrb	GTGGTCCTTACCGTCATCTCTC	GTGGAGTCGTAAGGCAACTGCA
Dll1	GCTGGAAGTAGATGAGTGTGCTC	CACAGACCTTGCCATAGAAGCC
Dll4	GGGTCCAGTTATGCCTGCGAAT	TTCGGCTTGGACCTCTGTTCAG
Jag1	TGCGTGGTCAATGGAGACTCCT	TCGCACCGATACCAGTTGTCTC
Jag2	CGCTGCTATGACCTGGTCAATG	TGTAGGCGTCACACTGGAACTC
Notch1	GCTGCCTCTTTGATGGCTTCGA	CACATTCGGCACTGTTACAGCC
Notch2	CCACCTGCAATGACTTCATCGG	TCGATGCAGGTGCCTCCATTCT
Notch3	GGTAGTCACTGTGAACACGAGG	CAACTGTCACCAGCATAGCCAG
Notch4	GGAGATGTGGATGAGTGTCTGG	TGGCTCTGACAGAGGTCCATCT
Angpt1	AACCGAGCCTACTCACAGTACG	GCATCCTTCGTGCTGAAATCGG
Angpt2	GCATGACCTAATGGAGACCGTC	GATAGCAACCGAGCTCTTGGAG
Shh	ACCCAACTCCGATGTGTTCCGTTA	TATATAACCTTGCCTGCCGCTGCT
Ihh	CGGCTTCGACTGGGTGTATTAC	AGGAAAGCAGCCACCTGTCTTG
Sphk1	GCTTCTGTGAACCACTATGCTGG	ACTGAGCACAGAATAGAGCCGC
S1pr1	CGCAGTTCTGAGAAGTCTCTGG	GGATGTCACAGGTCTTCGCCTT
Apln	AAAGCTTGCACAAATAGGCCCTGG	TTCCTAGCCACCCGCTTCACTAAA
Aplnr	GCCATTTCCGAAAGGAGCGCAT	CTTCACCAGGTGGTAAGGCATC

ImmunoResearch Laboratories) or horseradish peroxidase-conjugated donkey anti-goat IgG (sc-2020, Santa Cruz Biotechnology). Diaminobenzidine (Vector Laboratories) or red alkaline phosphatase substrate (Vector Laboratories) were the chromogens, and sections were counterstained with Harris' hematoxylin. Vessel density and coverage by mural cells were quantified using Northern Eclipse software. Apoptosis was detected using the In Situ Cell Death Detection Kit, Fluorescein (Roche Applied Science). OCT-embedded frozen sections were labeled with rat anti-mouse PDGFRβ monoclonal antibody (Clone APB5, eBioscience), rabbit anti-CD31 polyclonal antibody (Thermo Scientific), and rabbit anti-NG2 polyclonal antibody (EMD Millipore). Bound primary antibodies were visualized using biotinylated goat anti-rat IgG (Vector Laboratories), Dylight 549-conjugated streptavidin (Vector Laboratories), Alexa Fluor 488-conjugated goat anti-rabbit IgG (Life Technologies), and Alexa Fluor 594-conjugated goat anti-rabbit IgG. Nuclei were visualized with DAPI.

Cell Migration Assessment by Time-lapse Microscopy—Motility of Renca plated at 4,000 cells/cm^2 was assessed by time-lapse microscopy, as described previously (24, 25), using a Leica DMI6000 B microscope with IMC optics. Images were acquired every 5 min over 8 h using time-lapse software (Leica Application Suite).

Transmission Electron Microscopy—Tumor samples were fixed in 2% glutaraldehyde in PBS, pH 7.2, post fixed in 1% osmium tetroxide in PBS, dehydrated through a graded ethanol series, and embedded in epon-aradite. Ultra-thin sections stained with Reynold's lead citrate and 2% alcoholic uranyl acetate were examined and photographed with a Philips model 410 electron microscope at 60 kilovolts. Microvessel basement membrane thickness was measured at 20 sites/vessel, at equidistant locations around the vessel perimeter, using the line measurement tool in ImageJ software.

Laser Capture Microdissection—Kidney tumors were manually dissected, embedded in OCT compound (Tissue-Tek), snap-frozen in liquid nitrogen, and 10-μm sections were cut onto pre-chilled glass slides. The central quarter of the tumor area was microdissected by laser capture (Arcturus Veritas LCM System, Life Technologies) and RNA was extracted and quantified, as described previously (26).

Intravital Microscopy—Tumor-bearing BALB/c mice were anesthetized with inhaled isoflurane, the kidney tumor was exteriorized and placed within the central recess of a custom-built transparent plexiglass chamber positioned on the stage of an inverted microscope (IX81, Olympus) and kept moist by filling the chamber with 0.5 ml of 37 °C Krebs physiological salt solution, pH 7.4. Blood flow in the tumor was visualized by either ultraviolet epi-illumination (DAPI U-MWU2: 330–385 nm excitation filter, 420 nm emission filter) or blue light epi-illumination (U-MWIBA2: 460–490 nm excitation filter, 510–550 nm emission filter) following intravenous tail vein administration of FITC-labeled dextran (2×10^6 M_r; 20 mg/ml, 50 μl, Sigma). Images were acquired using a cooled coupled device camera (Rolera-XR, QImaging) at a rate of 21 images/s. Live image sequences were digitized and stored as uncompressed AVI movie files using custom frame capture software (NeoVision) and in-house software written in the MATLAB (Mathworks) programming environment. Offline analysis of movie files was conducted using ImageJ (NIH) software to quantify the vascular network morphometry of at least 10 random fields of view, in both control and FGF9-exposed tumors. Vascular length density was determined by manual tracing of all vessel centerlines and total network length was expressed relative to tumor area. Branch point density was determined by manual point counting of all vascular bifurcations and expressed as total bifurcations relative to total network length. Lumen diameter was determined by manually quantifying widths of individ-

ual vessels, perpendicular to the vessel centerline. Capillaries were defined as vessels with single-file red blood cell flow. Microcirculatory units were defined as flow routes in which red cells flowed from an arteriole-like vessel into one or more capillaries that drained into a venous structure characterized by slower flow than the feeding arteriole. Simple microcirculatory units were defined as those with a single capillary between an arteriole-venule pair and complex microcirculatory units were those with two or more capillaries between the pair. Vasoreactivity was assessed in arteries 20–60 μm in diameter fields, assessing the entire exposed tumor surface, at baseline and following administration of phenylephrine (Sigma, 1×10^{-6} M), after flushing with Kreb's solution and administering potassium chloride (KCl, 1×10^{-2} M), and after flushing with Kreb's solution and administering sodium nitroprusside (SNP) (1×10^{-7} M).

Detection of Tumor Hypoxia—Hypoxic tumor regions were identified by immunohistochemical detection of pimonidazole adducts, following tail vein injection of pimonidazole hydrochloride (60 mg/kg, Hydroxyprobe-1 Kit, Hydroxyprobe Inc.). Renal tissues were harvested 30 min after Hydroxyprobe-1 administration and 4-μm formalin-fixed paraffin-embedded sections were immunostained with a monoclonal mouse anti-pimonidazole antibody (Hydroxyprobe-1 mAb, 1:200) and the signal detected according to the manufacturer's protocol with diaminobenzidine color detection. Tumor sections were scanned (Aperio Scanscope CS system) and imported into MATLAB (MathWorks). The hypoxia signal was quantified from the yellow channel of the CMYK color mode. For display purposes, the image intensity range was compressed in Photoshop (Adobe), using an identical scale (83–223) for control and FGF9-expressing tumor samples. Hypoxic area was quantified as a percentage of total tumor area and hypoxic intensity as the mean raw signal intensity. The hypoxic gradient was defined as the slope of the linear regression line from the non-hypoxic edge of the hypoxic zone to the edge of the plateau signal from the most intensely stained hypoxia zone.

Cell Isolation by Magnetic Beads—Renal tumors were harvested, minced, and digested with Collagenase II (2 mg/ml, Worthington) in M199 at 37 °C for 40 min. After filtering through a 70-μm pore cell strainer (Corning Life Sciences) the suspension was incubated with Dynabeads (Life Technologies) pre-coated with rat anti-PDGFRβ monoclonal antibody (eBioscience) for 30 min at 4 °C. Bead-bound cells were cultured in DMEM with 10% FBS and bead-free cells incubated with Dynabeads pre-coated with rat anti-CD31 monoclonal antibody. The bead-bound CD31-positive cells were cultured in DMEM with 20% FBS, 100 μg/ml of endothelial cell growth supplements (E2759, Sigma), 100 μg/ml of heparin (H3149, Sigma), and non-essential amino acids (Life Technologies). The unbound PDGFRβ- and CD31-negative tumor cells were cultured in DMEM with 10% FBS. Growth curves were ascertained for cells in passages 2 and 3.

Local Delivery of Anti-PDGFRβ Antibody to Renal Tumors—Seven days after Renca cell implantation, mice were anesthetized with isoflurane and the left kidney and associated tumor were re-exposed. Rat monoclonal PDGFRβ blocking antibody (16-1402-82, eBioscience) or rat IgG2aκ isotype-matched control (16-4321-82, eBioscience) were diluted to 50 μg/ml in 30% Pluronic F-127 gel (Sigma) and the gel was then applied to the tumor surface with two sequential applications, 30 s apart, using a fine brush. After 3 days the tumors were subjected to either intravital microscopy, for assessment of tumor vessel architecture and vasoreactivity, or fixed and evaluated immunohistologically, as above. Histological assessments were restricted to the zone within 500 μm from tumor surface.

Statistics—Statistical analyses were performed using Prism 5 (GraphPad software). Values are presented as mean ± S.E. Groups were compared by two-tailed *t* test and cell growth data were compared by two-way analysis of variance with a Bonferroni post hoc test. Comparison of capillary diameters, which were not normally distributed, was undertaken using Mann-Whitney testing. Frequencies of capillaries positioned between arterioles and venules and arteries displaying vasoreactivity were compared using Fisher's exact test.

Results

FGF9 Suppresses Metastases of Renal Tumors in Mice—To investigate the impact of FGF9 delivery on tumor vessels, we sought to study a tumor in which FGF9 would have little to no direct effect on the tumor cells themselves. Renal tumors have not been prominently associated with FGF signaling and there is no evidence for FGF9 signaling in the pathogenesis of renal cancer (27, 28). Therefore, we assessed the renal adenocarcinoma cell line, Renca, for its responsiveness to FGF9. We first identified that Renca cells were relatively deficient in the IIIc isoforms of FGFR2 and FGFR3, receptors known to be potently activated by FGF9 (29) (Fig. 1*A*). In comparison, these receptors were relatively abundant in primary mouse dermal fibroblasts, which is consistent with the mesenchymal cell selectivity described for FGF9 (29, 30). We also found that stimulation of Renca cells with FGF9 resulted in minimal activation of ERK1/2, assessed by Western blot analysis, whereas dermal fibroblasts, mouse embryo fibroblasts, and the pericyte-like line 10T1/2 showed robust activation (Fig. 1*B*). In contrast, FGF2 did activate ERK1/2 in Renca cells (Fig. 1*C*). In addition, incubation of Renca cells with FGF9 did not stimulate their proliferation but did drive proliferation of mouse dermal fibroblasts and 10T1/2 cells (Fig. 1*D*). Transduction of adenovirus containing FGF9 cDNA into Renca cells also failed to induce proliferation (Fig. 1*D*). Similarly, whereas FGF9 suppressed serum withdrawal-induced apoptosis in dermal fibroblasts, there was no effect on Renca cells (Fig. 1*E*). Finally, time-lapse microscopy showed no effect of FGF9 on Renca cell migration, whereas it stimulated a 42% increase in migration speed of dermal fibroblasts (Fig. 1*F*).

We next generated renal tumors by orthotopically implanting Renca cells, expressing either human FGF9 or GFP, in the kidney subcapsular space of female BALB/c mice. This yielded rapidly expanding local tumors. FGF9 expression was detected in Renca-FGF9 tumors for at least 14 days but FGF9 was not detected in control, Renca-GFP tumors (Fig. 2*A*). FGF9-exposed tumors at 14 days were of similar weight as control tumors ($p = 0.890$, Fig. 2, *A* and *B*). As well, the proportion of Ki-67-positive cells was similar in GFP- and FGF9-exposed tumors, consistent with the lack of *in vitro* Renca cell prolifer-

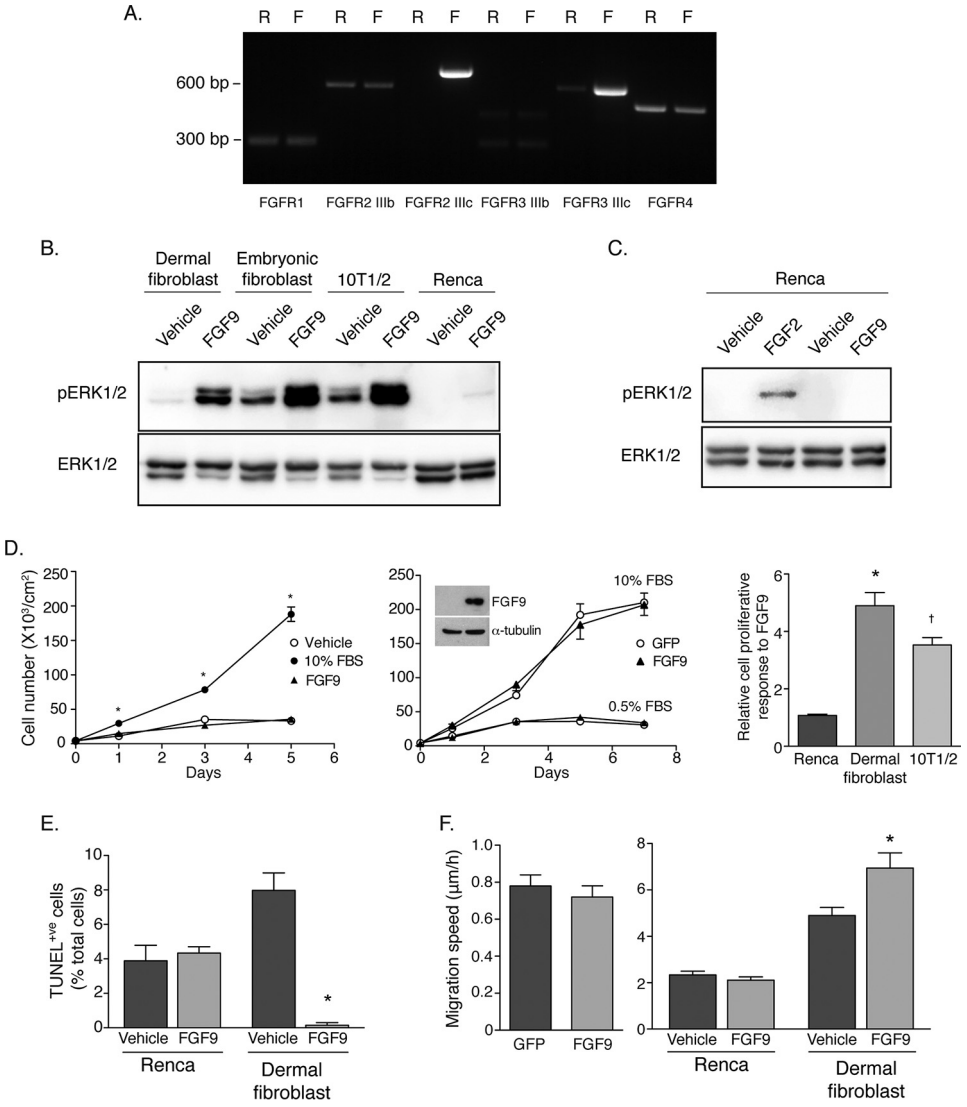

FIGURE 1. **FGF9 does not affect the proliferation or migration of Renca cells.** *A,* SYBRSafe-stained agarose gel depicting RT-PCR transcripts in Renca cells (*R*) and primary mouse dermal fibroblasts (*F*) for FGF receptors. *B,* Western blots of phosphorylated and total ERK1/2 in mouse dermal fibroblasts, mouse embryonic fibroblasts, 10T1/2 cells, and Renca cells subjected to 50 ng/ml of recombinant FGF9 or vehicle for 10 min. *C,* Western blots of phosphorylated and total ERK1/2 in Renca cells subjected to 50 ng/ml of recombinant FGF2 or FGF9 for 10 min. *D, left,* population growth of Renca cells in RPMI 1640 incubated with FGF9 (50 ng/ml) and 0.5% FBS, with PBS and 0.5% FBS, or with 10% FBS. $p < 0.001$. *Middle,* population growth of Renca cells transduced with adenovirus containing cDNA encoding either human FGF9 or GFP and cultured in medium with 0.5 or 10% FBS. Cell numbers were quantified in triplicate wells over 7 days. Western blots of cells harvested 48 h after transduction are shown. *Right*, proliferation response to FGF9 of Renca cells, dermal fibroblasts, and 10T1/2 cells, relative to that of vehicle. *, $p < 0.001$ *versus* Renca cells; †, $p = 0.004$ *versus* Renca cells. *E,* apoptosis of Renca cells and mouse dermal fibroblasts in 0.5% FBS-containing medium for 2 days, as assessed by TUNEL assay. *, $p < 0.001$ *versus* vehicle. *F,* migration speed of Renca cells transduced with adenovirus encoding GFP or FGF9 (*left*) and of Renca cells and mouse dermal fibroblasts in vehicle or recombinant FGF9 (50 ng/ml) (*right*), as assessed by time-lapse microscopy. *, $p = 0.036$ *versus* vehicle.

ation by FGF9. Likewise, there was no difference in TUNEL positivity (Fig. 2*C*). Remarkably, however, assessment of lung metastases revealed substantially fewer tumor foci on the surfaces of lungs of mice bearing FGF9-expressing tumors ($p = 0.029$, Fig. 2, *D* and *E*). Similarly, the density of tumor foci in lung cross-sections was reduced ($p = 0.004$) and diameters of the metastatic foci were significantly smaller ($p = 0.019$, Fig. 2, *E* and *F*).

FGF9 Fortifies the Vasculature in Renal Tumors—The FGF receptor profile in Renca cells and the lack of an effect of FGF9 on Renca cell replication and migration suggested that the suppression of metastases was not a direct effect of FGF9 on tumor cells. We therefore assessed if the vasculature could be implicated. Microvessels were readily detectable in 14-day-old tumors, based on hematoxylin and eosin staining. Immunostaining revealed that >90% of these vessels were lined by CD31-positive endothelial cells. Interestingly, there was no evidence that FGF9 stimulated angiogenesis in the renal tumor. In fact, FGF9-expressing tumors contained 17% fewer CD31-expressing blood vessels than GFP-expressing tumors ($p = 0.003$, Fig. 3*E*).

We next tested whether FGF9 stimulation affected the integrity of the vasculature within the tumor. Pericytes are central to microvascular stability and we quantified pericyte abundance by immunostaining the tumors for NG2. This revealed that FGF9 exposure almost quadrupled the proportion of vessels

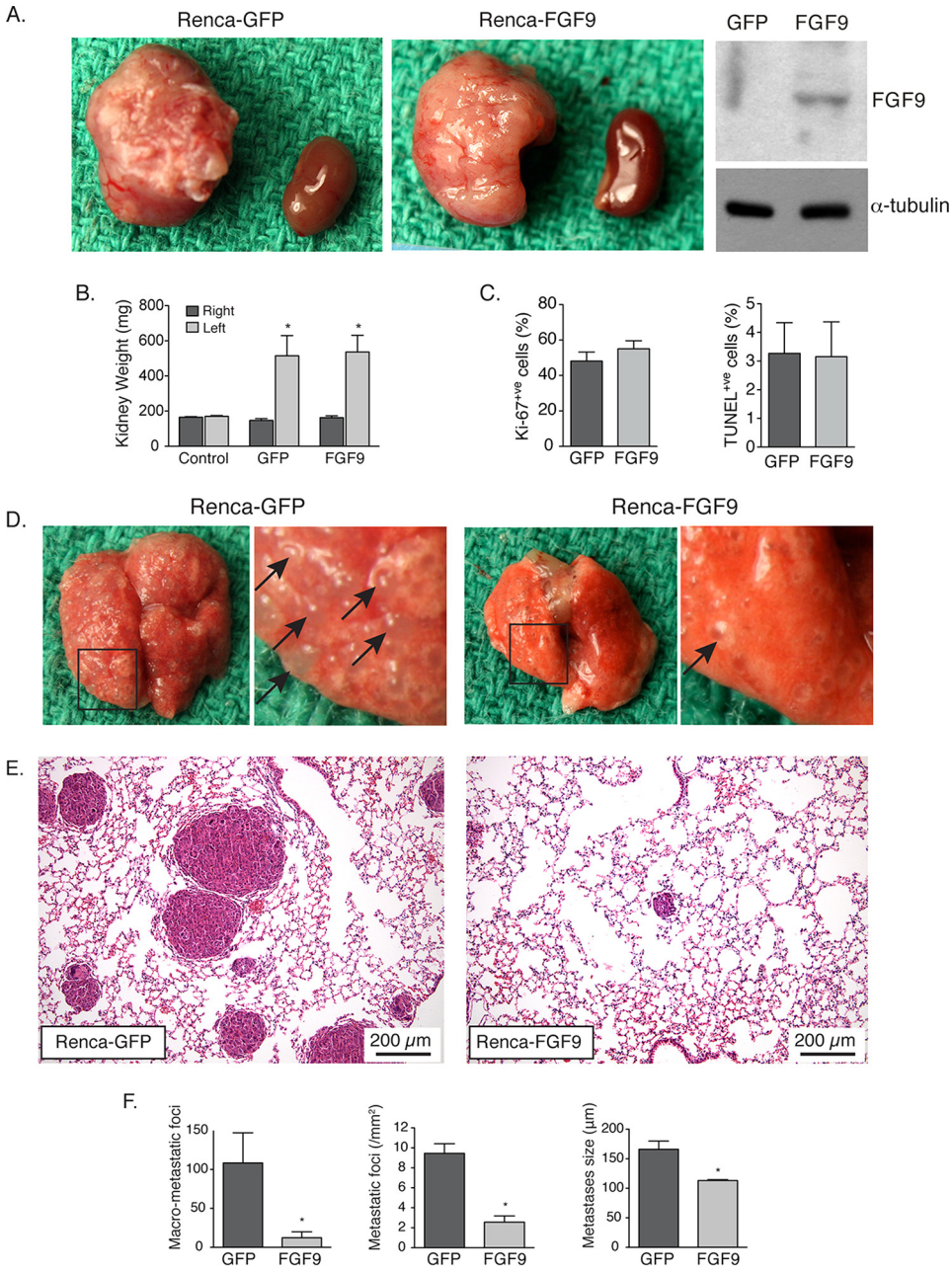

FIGURE 2. **FGF9 suppresses metastasis of Renca cell-derived renal tumors.** *A,* photographs of kidney tumors harvested 14 days after renal subcapsular injection of Renca cells expressing either GFP or FGF9 in growth factor-reduced Matrigel. The corresponding, non-injected contralateral kidney is shown on the *right* of each photograph. Western blot showing detectable FGF9 expression Renca-FGF9 tumor is shown on the *right*. *B,* graph of kidney weights. *, $p = 0.010$ for GFP-expressing tumor *versus* right kidney; *, $p = 0.003$ for FGF9-expressing tumor *versus* right kidney; $p = 0.89$ for GFP- *versus* FGF9-expressing tumor ($n = 6$). *C,* graphs depicting the proliferation (*left*) and apoptosis (*right*) in renal tumors, as assessed by immunostaining for Ki-67 and TUNEL assay, respectively. *D,* micrographs of lungs harvested from mice 14 days after renal injection of Renca cells expressing GFP or FGF9. Macrometastases are evident as translucent distensions on the lung surface, with selected lesions in a digitally magnified region (*box*) depicted by the *arrows*. *E,* photomicrographs of 5-μm formalin-fixed lung sections stained with hematoxylin and eosin showing metastatic foci within lung parenchyma. *F,* graphs depicting the mean number of surface macrometastases (*, $p = 0.029$), the density of intrapulmonary metastases (*, $p = 0.004$), and the size of metastatic foci (*, $p = 0.019$) in control and FGF9-expressing tumors.

associated with NG2-positive pericytes ($p = 0.015$) (Fig. 3, *A*, *B*, and *E*). We also immunostained for SM α-actin-expressing cells and found that the otherwise low proportion of vessels surrounded by SM α-actin-expressing cells (0.6 ± 0.4%) increased 13.8-fold ($p = 0.002$) (Fig. 3, *C–E*). Moreover, SM α-actin-positive vessels in FGF9-exposed tumors were characterized by circular lumen cross-sections typical of arterioles, in contrast to the collapsed, or alternatively dilated and irregular, vessel lumens found in control tumors (Fig. 3, *C* and *D*).

To further delineate the perivascular architecture, we undertook transmission electron microscopy. In control tumors, endothelial cells were directly adjacent to tumor cells (Fig. 3*F*). However, in FGF9-expressing tumors the tumor cells were typically separated from the endothelial cells by pericytes or vascular SMCs (Fig. 3, *G–I*). As well, the capillary endothelial basement membrane in FGF9-expressing tumors was more continuous (Fig. 3*G*) and 2.5-fold thicker ($p = 0.017$) than in control tumors (Fig. 3*J*). Interestingly, the basement membrane

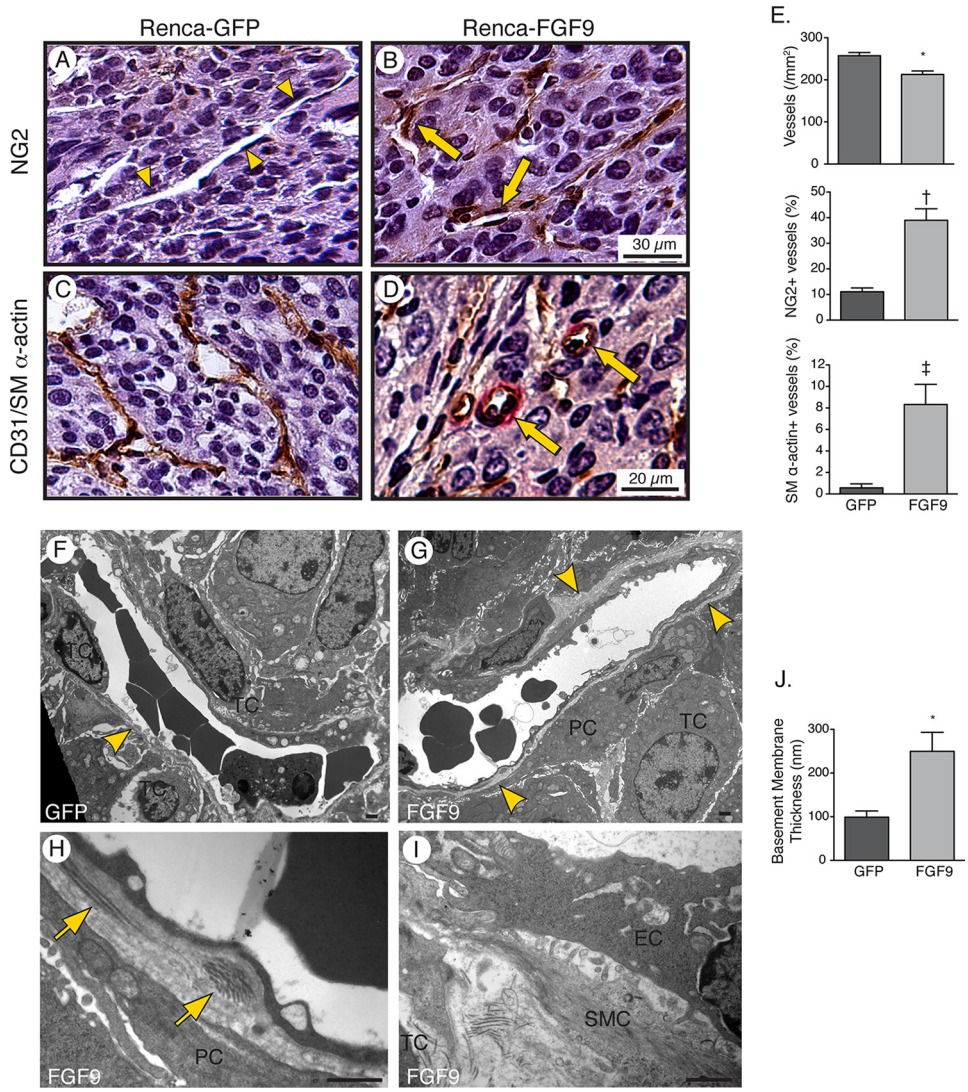

FIGURE 3. **FGF9 stimulates recruitment of vascular mural cells and deposition of a reinforced basement membrane.** *A–D*, photomicrographs of 5-μm Tris-buffered zinc-fixed renal tumor sections harvested 14 days after renal injection of Renca cells expressing GFP and FGF9 and immunostained for NG2-positive pericytes (*A* and *B*) or CD31 (*brown*) and SM α-actin (*red*) (*C* and *D*). *Arrowheads* depict microvessel devoid of NG2-positive pericytes and *arrows* depict microvessels invested by pericytes. Some SM α-actin-positive microvessels have an arteriolar morphology (*arrows*). *E,* graphs depicting the density of microvessels (*, $p = 0.003$), percentage of microvessels invested with NG2-postive pericytes (†, $p = 0.015$), and percentage of microvessels associated with SM α-actin expressing cells (‡, $p = 0.002$), $n = 6$. *F–I*, transmission electron micrographs of microvessels showing an incomplete endothelial basement membrane (*BM*, *arrowhead*), with encroaching tumor cells (*TC*), in a 14-day GFP-expressing tumor (*F*). A circumferential basement membrane exists in the FGF9-expressing tumor (*G*, *arrowheads*) with pericytes (*PC*) and SMCs separating tumor cells from the vessel (*G–I*). *Arrows* depict fibrillar collagen deposits in the basement membrane. EC, endothelial cell. *Bar*, 1 μm. *J,* graph depicting the mean thickness of the basement membrane of tumor microvessels, measured from 25 microvessels in GFP-expressing tumors and 20 vessels in FGF9-expressing tumors (*, $p = 0.017$).

in FGF9-expressing tumors also contained foci of fibrillar collagen, effectively "spiking" it with the mechanically strong collagen type (Fig. 3*H*). Collectively, these data establish that FGF9 can drive a microvessel maturation program in renal tumors, without stimulating angiogenesis, and that this program entails vessel fortification by pericytes, SMCs, and an enriched basement membrane.

FGF9 Normalizes Microvascular Network Architecture and Flow Routes—In addition to having thin walls, tumor vessels are characterized by a highly branched and chaotic arrangement of channels with little resemblance to the ordered network present in normal tissues (5). We thus questioned whether FGF9 would impact the network architecture. To study the vessel network in renal tumors, we developed a real-time microvessel visualization approach by exteriorizing the tumor and imaging red blood cell flow by intravital microscopy. This revealed striking architectural changes imparted by FGF9. Whereas vessels in control tumors were densely packed and highly branched, those in FGF9-expressing tumors were more spaced and less chaotic (Fig. 4, *A* and *B*). Quantitative analysis revealed a reduction in the vessel length density (33%, $p = 0.034$), a 67% reduction in mean lumen diameter ($p < 0.001$), and 57% fewer branch points ($p = 0.019$) (Fig. 4, *A–C*).

Intravital microscopy also enabled tracking the transit of red cells within the network. Red cell flow was profoundly disordered in control tumors, with seemingly random movement from channel to channel (Fig. 4*D*, supplemental Video S1). As well, transitions in vessel caliber were non-progressive (*e.g.* large-smaller-larger), with substantial step changes in lumen diameter (Fig. 4*E*, supplemental Videos S2 and S3). In contrast,

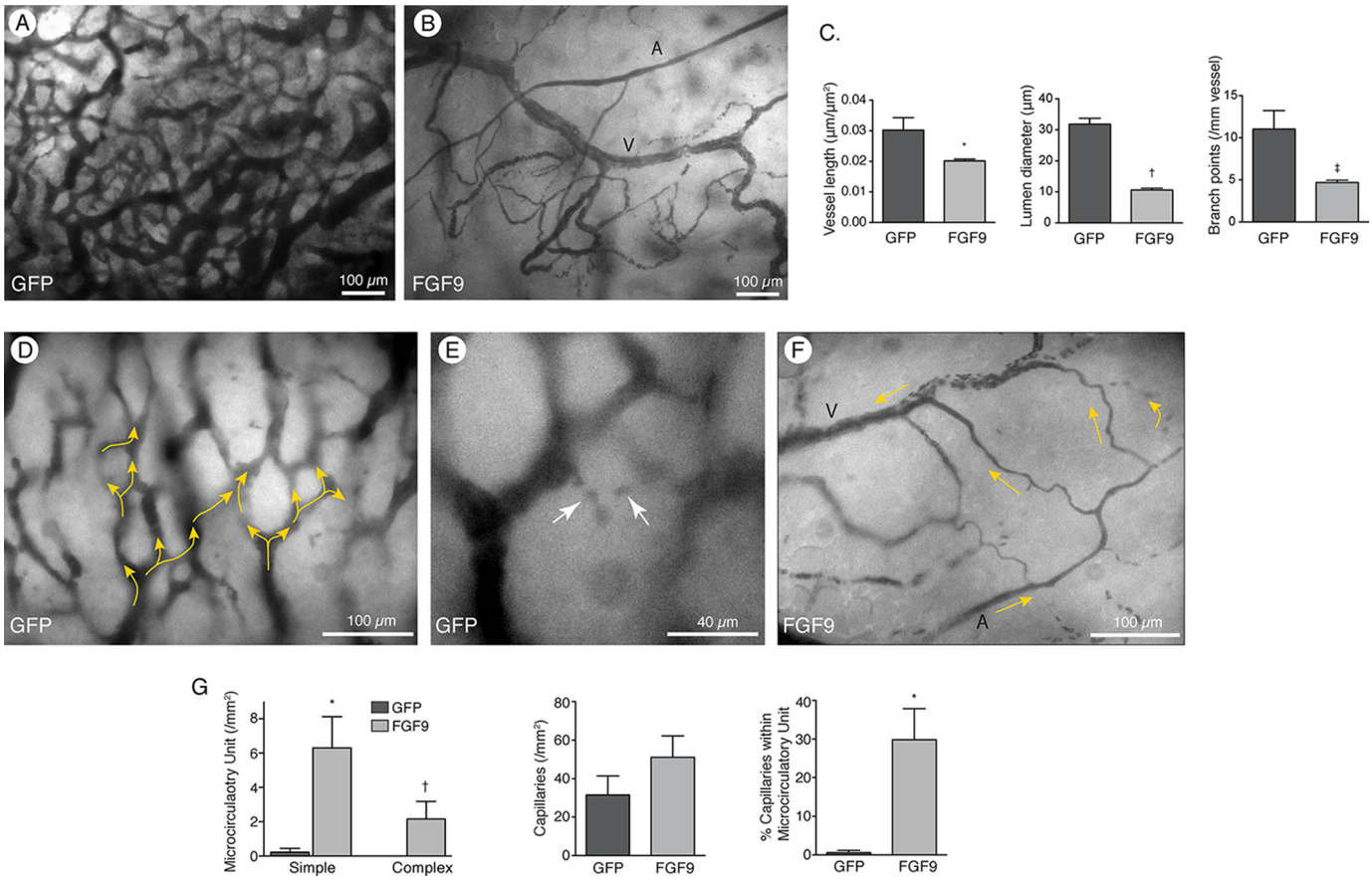

FIGURE 4. **FGF9 imparts hierarchy to the tumor vasculature.** *A* and *B*, ultraviolet fluorescence intravital microscopy images of red blood cells flowing within the vasculature of GFP-expressing (*A*) and FGF9-expressing (*B*) renal tumors 14 days after injection of Renca cells. GFP-expressing tumors (*A*) show a densely packed network of highly branched vessels. The network in FGF9-expressing tumors (*B*) is less dense and less branched. There is also a "smooth" appearance to some vessels in FGF9-expressing tumors, consistent with faster flow in an arterialized vessel (*A*), and a more irregular appearance in other vessels, with cell-free spaces in the lumen, consistent with slower flow in a venous structure (*V*). *C*, graphs depicting vascular length density (*, $p = 0.034$), lumen diameter (*, $p < 0.001$), and branch point density (*, $p = 0.019$). At least 10 fields of view were averaged for each mouse, with 3 GFP-expressing tumors and 4 FGF9-expressing tumors. *D–F*, higher magnification intravital images illustrating chaotic and serpentine flow routes (*D*, *yellow arrows*) and orphaned capillaries (*E*, *white arrows*) in GFP-expressing tumors, but ordered flow through an arterial-capillary-venous microcirculatory unit in an FGF9-expressing tumor (*F*). *Arrows* depict flow routes. *C*, capillary. *G*, graphs depicting the density of simple and complex microcirculatory units of arterial to capillary to venous flow (*, $p < 0.001$; †, $p = 0.007$), capillary density defined as vessels with single file red blood cell flow ($p = 0.233$), and percentage of capillaries positioned within a microcirculatory unit (*, $p = 0.028$). Movies corresponding to images in *panels D*, *E*, and *F* can be found in supplemental Videos S1, S3, and S4, respectively. Supplemental Video S2 depicts another example of bizarre step changes in lumen diameter and absence of flow hierarchy.

in FGF9-expressing tumors we identified discrete, hierarchical microcirculatory units. In these units, red cells flowed through gradually and progressively smaller caliber vessels, entered one or more capillaries, and then drained into a collecting venule (Fig. 4*F*, supplemental Video S4). Notably, within capillaries red blood cells transited in single file, with plasma gaps between each cell (Fig. 4*F*, supplemental Video S4). By this definition, capillaries were rare in control tumors. Moreover, those that were identified were effectively orphaned, with no evidence for a feeder arteriole or a draining venule. Instead, they were bizarrely situated between two large caliber venous-like channels (Fig. 4*E*, supplemental Videos S2 and S3). In contrast, 30% of capillaries in FGF9-expressing tumors were appropriately positioned within a bona fide microcirculatory unit ($p = 0.028$, Fig. 4*G*).

FGF9 Generates a Vasoreactive Tumor Vasculature—We next sought to determine whether the FGF9-modified microvascular tree was capable of regulating flow through vasoreactivity. Ten days after implantation of GFP- or FGF9-expressing tumor cells, mice received a systemic injection of FITC-conjugated high molecular weight dextran, vessels were imaged by intravital microscopy, and phenylephrine (1×10^{-5} M), KCl (1×10^{-2} M), and sodium nitroprusside (1×10^{-7} M) were sequentially administered. By recording video frames of the entire exposed surface, we ascertained that although vasoresponsiveness was not evident in the control tumors, it was present at sites throughout FGF9-expressing tumors. In some vessels, discrete sites of vasoconstriction developed in response to phenylephrine. Constriction increased upon KCl delivery with more diffuse lumen narrow. After SNP, these changes were almost completely reversed (Fig. 4*A*, *top*). In regions where a tapered arterial tree was present, vasoconstriction was associated with complete cessation of flow in one or more of the arterial branches. This was coupled to a corresponding diffuse loss of FITC signal, suggesting reduced perfusion to the region (Fig. 5*A*, *middle*, and supplemental Video S5). Quantitative analysis of all vessels between 20 and 60 μm in diameter that flowed into narrower caliber vessels confirmed a statistically significant acquisition of vasoreactivity in FGF9-expressing tumors (Fig. 5*B*). This ability to regulate flow through vasomo-

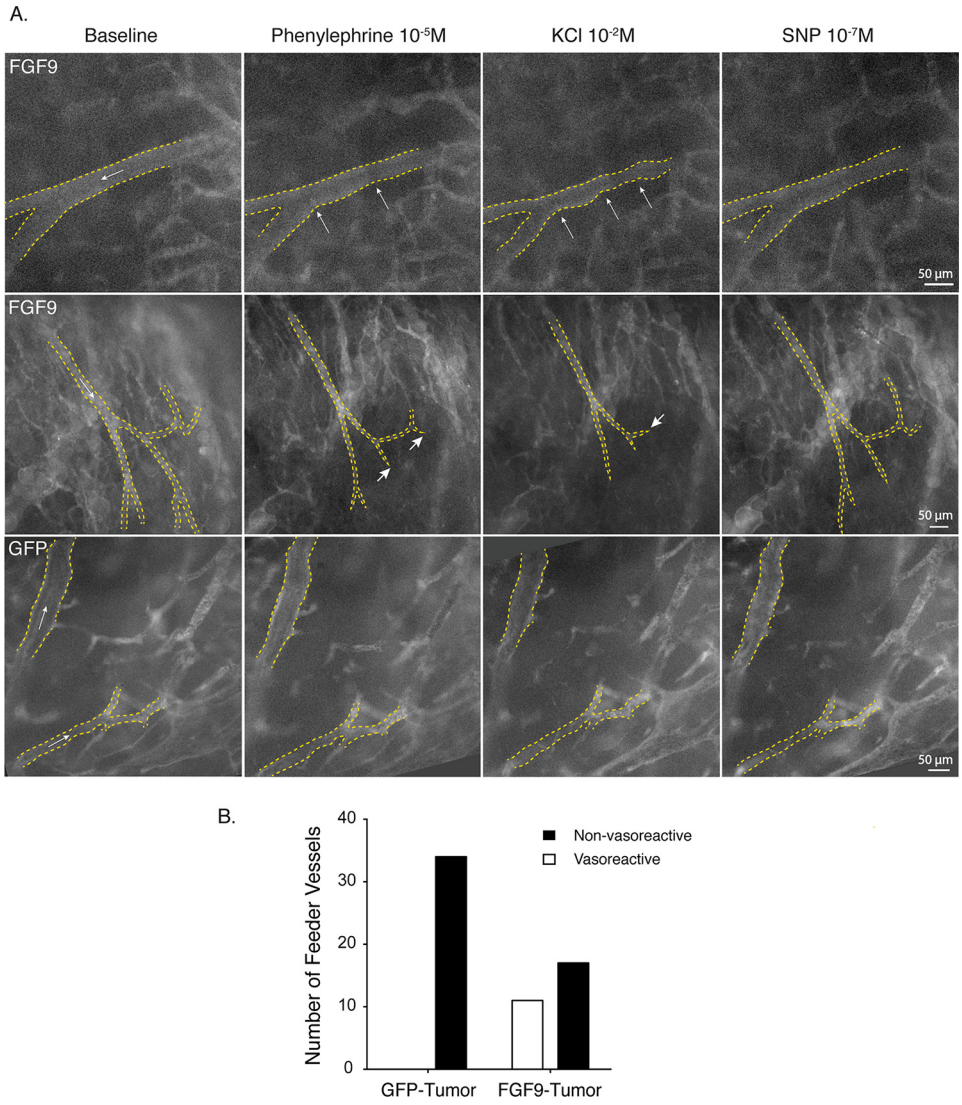

FIGURE 5. **FGF9 imparts tumor vessels with vasoreactivity.** *A*, intravital microscopy images of vessels within orthotopic renal tumors 10 days after injection of Renca cells, imaged live by intravital microscopy following injection of FITC-labeled dextran. Images depict the vascular lumen before and after subfusion of phenylephrine (10^{-5} M), KCl (10^{-2} M), and SNP (10^{-7} M), for a minimum of 3 min as indicated. *Arrows* within the lumen depict the direction of flow. *Top panel,* vessel within an FGF9-expressing tumor showing focal vasoconstriction (*arrows*) in response to phenylephrine subfusion, and both focal and diffuse constriction following KCl subfusion. The lumen diameter widens after subfusion with SNP. *Middle panel*, vessels within an FGF9-expressing tumor showing flow down a network with progressively smaller branches. Following phenylephrine subfusion, diffuse vessel constriction can be seen as well as complete cessation of flow in some of the distal vessel branches (*short arrows*). This is accompanied by a loss of fluorescence signal throughout the tumor, indicating widespread reduction in tumor perfusion. Diffuse vessel constriction, cessation of flow in distal vessels (*short arrow*), and generalized hypoperfusion are even more pronounced following KCl administration. These changes are partially reversed following delivery of SNP. *Bottom panel*, vessels within a GFP-expressing tumor showing no change in luminal diameter or flow indicators following delivery of vasomotor agents. *B,* plot of all vessels segments imaged, 20–70 μm in diameter and with continuous flow into progressively smaller branches, which displayed vasoreactivity. $n = 34$ and 28 vessels in GFP- and FGF9-expressing tumors, respectively. $p = 0.0085$. Movie corresponding to the *middle row* of images in *panel A* can be seen in supplemental Video S5.

tion, with intact α-adrenergic and nitric oxide signaling, represents a level of physiologic maturity not previously identified in tumor microvessels.

FGF9 Reduces Tumor Hypoxia—The combination of vessel hierarchy, capillaries with single file red blood cells, and vasoreactivity could substantially impact oxygen delivery in the tumor. To test this, we quantified hypoxia-induced adducts of infused pimonidazole. This revealed that the average intensity of the hypoxia signal in FGF9-modified tumors was 33% lower than that in control tumors ($p = 0.031$, Fig. 6). Interestingly, the total area of tumor that displayed any hypoxia signal was not altered by FGF9 ($p = 0.755$), however, oxygenation of the tumor core was substantially improved. Regional signal intensity analysis revealed that control tumors displayed a steep gradient of hypoxia toward the central zone, whereas FGF9-exposed tumors displayed homogeneous, low-intensity hypoxia ($p = 0.010$).

Hypoxia-induced up-regulation of VEGF is a primary driver of tumor angiogenesis, but because the resulting aberrant vasculature does not correct the hypoxia, VEGF expression continues unabated (31). To determine whether this unchecked cascade was halted by FGF9, we quantified expression of VEGF-A in the tumor core, harvesting this region by laser capture microscopy. This revealed a 35% reduction in VEGF-A transcript abundance in FGF9-expressing tumors compared with control tumors ($p = 0.031$). Thus, the FGF9-driven micro-

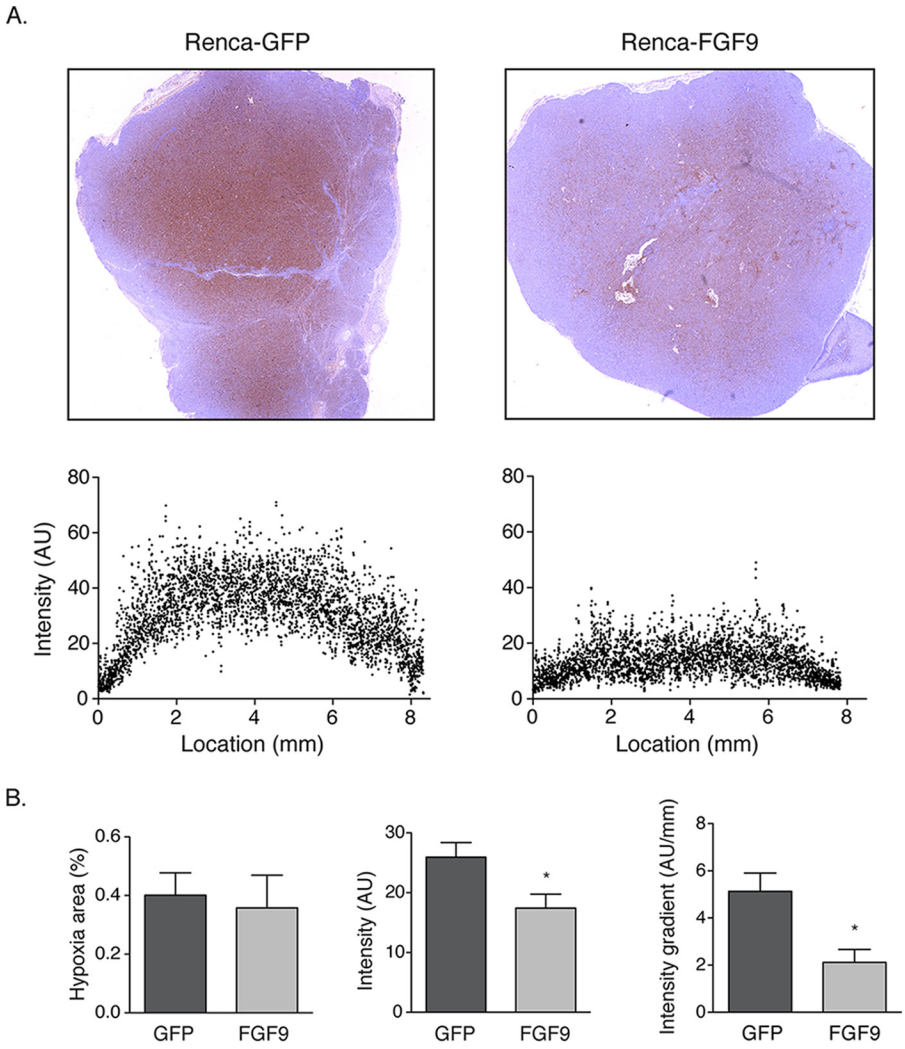

FIGURE 6. **FGF9 reduces tumor hypoxia.** *A,* photomicrographs of formalin-fixed sections of orthotopic mouse renal tumors harvested 14 days after Renca cell injection and 30 min after intravenous infusion of Hydroxyprobe-1. Sections were immunostained for pimonidazole adducts. To optimize contrast, the image intensity range was compressed in Photoshop (Adobe), using an identical scale (83–223) for control and FGF9-expressing tumor samples. *Line* profiles of the raw *yellow color* channel signal intensity extracted from a line across the tumors with the starting location (0 mm) at the edge of each tumor, depicting hypoxia signal intensity, are shown *below* the respective images. *B,* graphs depicting the hypoxic area (*, $p = 0.031$), mean hypoxic intensity signal (*, $p = 0.755$), and hypoxia gradient from the non-hypoxic region to the edge of the maximally hypoxic zone (*, $p = 0.010$), $n = 6$.

vascular reconfiguration improved tumor oxygenation, thereby suppressing a key driver of angiogenesis.

FGF9 Amplifies a PDGFRβ-positive Stromal Cell Population in Renal Tumors—To elucidate the mechanism by which FGF9 reconfigured the microvasculature, we undertook quantitative RT-PCR expression screening for 20 candidate vascular maturation genes in control and FGF9-exposed tumors. This revealed increased expression of components of the PDGF signaling pathway, including up-regulation of PDGFRβ (Table 2). PDGFRβ has been found to mark mesenchymal progenitor cells, including a perivascular population, and signaling through the PDGFRβ is necessary for the investment of blood vessels by mural cells (21, 32, 33). We validated the *in vivo* up-regulation of PDGFRβ by Western blot analysis (Fig. 7*A*). This was further supported by immunostaining, which revealed a 46% increase in PDGFRβ-positive (+) cells in the FGF9-expressing tumors ($p = 0.045$, Fig. 7, *B* and *C*). These cells were located within the tumor stroma, both associated and unassociated with a vessel wall. In some regions, chains of non-mural PDGFRβ$^+$ stromal cells were seen to connect with a microvessel, suggesting a vascular recruitment process (Fig. 7*B*). Double labeling for PDGFRβ and NG2 revealed that 81 ± 7% of the mural, PDGFRβ$^+$ cells in both control and FGF9-expressing tumors were also NG2-positive, indicating a pericyte identity (Fig. 7*D*). The proportion of microvessels invested by one or more pericytes/PDGFRβ$^+$ cells increased from 39.5 ± 3.8 to 52.6 ± 3.8% ($p = 0.028$) and the proportion of the vessel perimeter covered by PDGFRβ$^+$ cells increased from 11.4 ± 1.4 to 24.5 ± 2.2% ($p < 0.001$, Fig. 7*C*). We also found that the length of the contact interface between a single mural cell and the underlying endothelial cell increased by 70% ($p < 0.001$, Fig. 7*C*), indicating more intimate investment of the vasculature by PDGFRβ$^+$ mural cells.

We next sought to determine whether the increase in PDGFRβ expression was consistent with an amplified population of cells, *versus* an increase in PDGFRβ expression in preexisting stromal cells. To assess this, PDGFRβ-expressing cells were harvested from control renal tumors by magnetic bead

TABLE 2

Relative expression of selected vascular maturation genes in FGF9-expressing renal tumors

Abundance of transcripts in 14-day-old renal tumors expressing FGF9 was determined by SYBR Green real-time PCR and expressed relative to that in control renal tumors.

Gene	Fold-change	*p* value
	mean ± S.D.	
Pdgfb	1.52 ± 0.30	**0.037**
Pdgfd	1.46 ± 0.20	**0.014**
Pdgfra	1.44 ± 0.26	**0.043**
Pdgfrb	1.57 ± 0.24	**0.015**
Dll1	0.92 ± 0.39	0.817
Dll4	1.18 ± 0.36	0.494
Jag1	1.02 ± 0.26	0.941
Jag2	1.19 ± 0.29	0.402
Notch1	1.66 ± 0.29	**0.031**
Notch2	1.61 ± 0.33	**0.044**
Notch3	1.06 ± 0.43	0.886
Notch4	1.03 ± 0.47	0.936
Shh	1.47 ± 0.25	**0.049**
Ihh	0.53 ± 0.14	0.087
Sphk1	1.03 ± 0.34	0.931
S1pr1	1.15 ± 0.31	0.470
Apln	1.03 ± 0.34	0.920
Aplnr	1.12 ± 0.48	0.697
Efnb2	1.03 ± 0.38	0.939
Ephb4	0.96 ± 0.17	0.774

isolation. Immunostaining of resulting cultures revealed that >80% also expressed NG2. Incubation of PDGFRβ-positive cells with FGF9 (50 ng/ml) yielded a 40% increase in their proliferation rate ($p = 0.002$, Fig. 7*E*). In contrast, FGF9 had no effect on the proliferation of $CD31^+$ endothelial cells isolated from the same tumors. FGF9 also had no impact on proliferation of PDGFRβ/$CD31^-$ double-negative cells, cells that closely resembled the original Renca cells pre-implantation. Together, these findings indicate that FGF9 directly amplifies a population of mesenchymal cells and suggest that these cells home to the neovasculature.

Local Inhibition of PDGFRβ Abrogates FGF9-driven Microvascular Network Differentiation and Tumor Passivation—Having identified an FGF9-sensitive, PDGFRβ-expressing stromal population we next asked if the PDGFRβ receptor itself mediated the FGF9-induced reshaping of the microvasculature. To test this, we applied Pluronic-F127 gel containing anti-PDGFRβ antibody, or isotype-matched IgG, to the surface of 7-day-old tumors and histologically assessed the vasculature deep to the application site 3 days later. This revealed that PDGFRβ blockade abrogated the FGF9-induced wrapping of vessels with NG2-expressing ($p = 0.006$) and SM-α-actin-expressing ($p = 0.038$) mural cells, yielding instead dilated vessels with thin walls (Fig. 8*A*).

We next evaluated the impact of PDGFRβ blockade on network architecture using the intravital microscopy-based assessment of the vascular network. Exposure of FGF9-exposed tumors to PDGFRβ blocking antibody yielded vessels that were significantly more dilated (2.0-fold, $p < 0.001$) and more branched (1.7-fold, $p = 0.003$). Furthermore, the number of capillaries in FGF9-exposed tumors was reduced by 57% ($p = 0.046$). In addition, by dynamically imaging vessel lumen caliber we found no evidence for constriction of microvessels in response to either phenylephrine or KCl in FGF9-exposed tumors subjected to PDGFRβ blockade (Fig. 8*B*). Finally, histological examination of the lungs of mice with FGF9-expressing tumors revealed that FGF9 failed to suppress metastases when the PDGFRβ in the primary tumor was blocked (Fig. 8*C*). Thus, the structural and functional actions of FGF9 on the tumor vasculature depended on a cascade of amplifying $PDGFR\beta^+$ stromal cells and on PDGFRβ-dependent recruitment of these cells to the vasculature.

Discussion

In this study, we demonstrate using an orthotopic renal tumor model that local delivery of FGF9 selectively and productively remodels the microvascular network. FGF9 did not stimulate blood vessel formation but, instead, transformed the otherwise thin-walled endothelial-lined channels into a fortified microvascular network with hierarchy and vasoreactivity. This uniquely matured microcirculatory system was associated with improved tumor oxygenation and reduced pulmonary metastases.

The paradigm of tumor vessel normalization has emerged in recent years and it is proposed that anti-angiogenesis therapies may confer their benefit, at least in part, through vessel normalization (8). To date, indicators of vessel normalization have included reduced vessel density, smaller caliber channels, enhanced endothelial integrity, and increased coverage by mural cells (8, 34–37). However, if the goal is to approximate the perfusion attributes of healthy tissue, there remains a substantial "gap" between the status of a post-anti-VEGF vasculature and that of healthy tissues. The current findings with FGF9 delivery indicate that this differentiation gap can be narrowed and that a physiologically advanced microcirculation in tumors is achievable.

Particularly striking was the emergence of a hierarchical network where fast flowing arterioles fed capillaries that drain into slow flowing venules. A degree of vascular network hierarchy has been suggested in glioblastomas treated with cedranib, as indicated by a mixture of high- and low-flow vessels (38). Hierarchy after anti-angiogenesis therapy in mice has also been suggested by improvements in tumor metabolism and drug delivery (13, 39). However, these changes in blood flow and drug delivery could also be due alterations in hydrostatic pressure (8). Moreover, the emergence of bona fide capillaries has not been identified. The current intravital, micron level assessment of the vasculature provides direct evidence that microcirculatory hierarchy can be obtained in tumors. FGF9 yielded a network with reduced vessel content, reduced vessel branching, and arteriole-capillary-venular units. This architecture provides a functional route for red blood cells, avoiding recycling of deoxygenated blood.

Real-time visualization of red blood cells enabled us to define capillaries as vessels in which red cell flow proceeded exclusively in single file. A seminal report by Tong and co-workers (11) described a reduction in vessel caliber in response to VEGFR2 blockade, with the emergence of more vessels below 20 μm in diameter. However, vessels in this size range can still accommodate simultaneous transit of multiple cells, unlike capillaries in normal tissues where diameters average 4–6 μm (16, 40). We determined that capillaries with single file red blood cell flow were rare in control tumors and most of those that were found were orphaned from arterioles. By contrast,

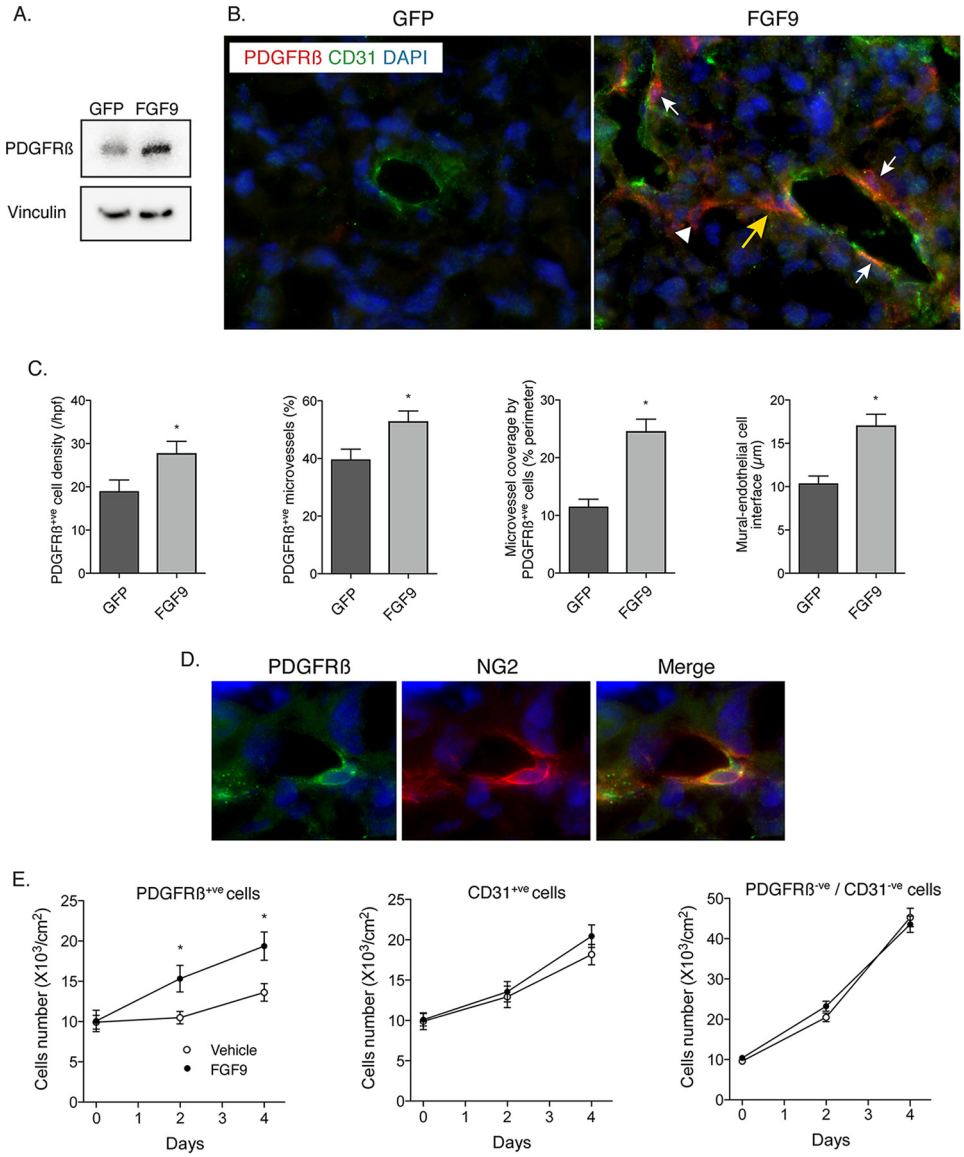

FIGURE 7. **FGF9 selectively amplifies PDGFRβ-positive stromal cells, which invest the tumor vasculature.** *A,* Western blots showing the abundance of PDGFRβ in GFP- and FGF9-expressing tumors. *B,* fluorescence micrographs of renal tumors harvested 14 days after Renca cell injection and double-immunostained for CD31 (*green*) and PDGFRβ (*red*), with nuclear detection using DAPI (*blue*). There are scant PDGFRβ-positive cells in the control, GFP tumor. In the FGF9-expressing tumor, PDGFRβ-positive cells can be seen wrapping blood vessels (*white arrows*), in the tumor stroma unassociated with vessels (*arrowhead*), and in a pattern suggesting directed migration toward the blood vessel wall (*yellow arrow*). *C,* graphs indicating the total content of PDGFRβ-positive cells (*, $p = 0.045$), the proportion of PDGFRβ-positive blood vessels within the tumors (*, $p = 0.028$), the fractional coverage of blood vessels by PDGFRβ-positive cells (*, $p < 0.001$), and the length of individual PDGFRβ-positive cells that have invested the blood vessel (*, $p < 0.001$). *D,* fluorescence micrographs of renal tumors double-immunolabeled for PDGFRβ (*green*) and NG2 (*red*), with nuclei stained with DAPI (*blue*). Distinct patterns of PDGFRβ and NG2 immunoreactivities in the same perivascular cell are evident. *E,* graphs depicting the proliferation of PDGFRβ-expressing cells (*left*) $CD31^+$ endothelial cells (*middle*), and PDGFRβ-negative/CD31-negative cells (*right*) harvested from renal tumors by magnetic bead isolation and incubated with FGF9 (50 ng/ml) or vehicle (*, $p = 0.002$).

FGF9 generated bona fide capillaries appropriately situated within microcirculatory units to optimize oxygen delivery.

Our finding of vasomotor competence in the microcirculation of FGF9-exposed tumors is also relevant to generating functional perfusion in tumors. Several integrated control systems regulate microvascular flow, including centrally initiated neural impulses, circulating hormonal factors, local myogenic responses, and retrograde conducted vascular signaling from local hypoxic cues (41, 42). The output from each of these cascades depends on the presence of functional SMCs around arterioles. It is notable therefore that SMCs were increased in FGF9-exposed tumors. Moreover the fact that arterial-caliber vessels in FGF9-exposed tumors contracted to an α-adrenergic stimulus and dilated in response to nitroprusside, with concomitant shifts in distal perfusion, reveals a previously unobserved competency in regulating microcirculatory flow. Although we cannot exclude the possibility that some of the vasoactive arteries were pre-existing vessels that became engulfed by the growing tumor, the widespread distribution of muscularized vessels and the emergence of vasoreactivity exclusively in FGF9-exposed tumors argues for maturation of *de novo* generated tumor blood vessels.

The reduced hypoxia in the tumor core of FGF9-exposed tumors was associated with suppressed VEGF expression in

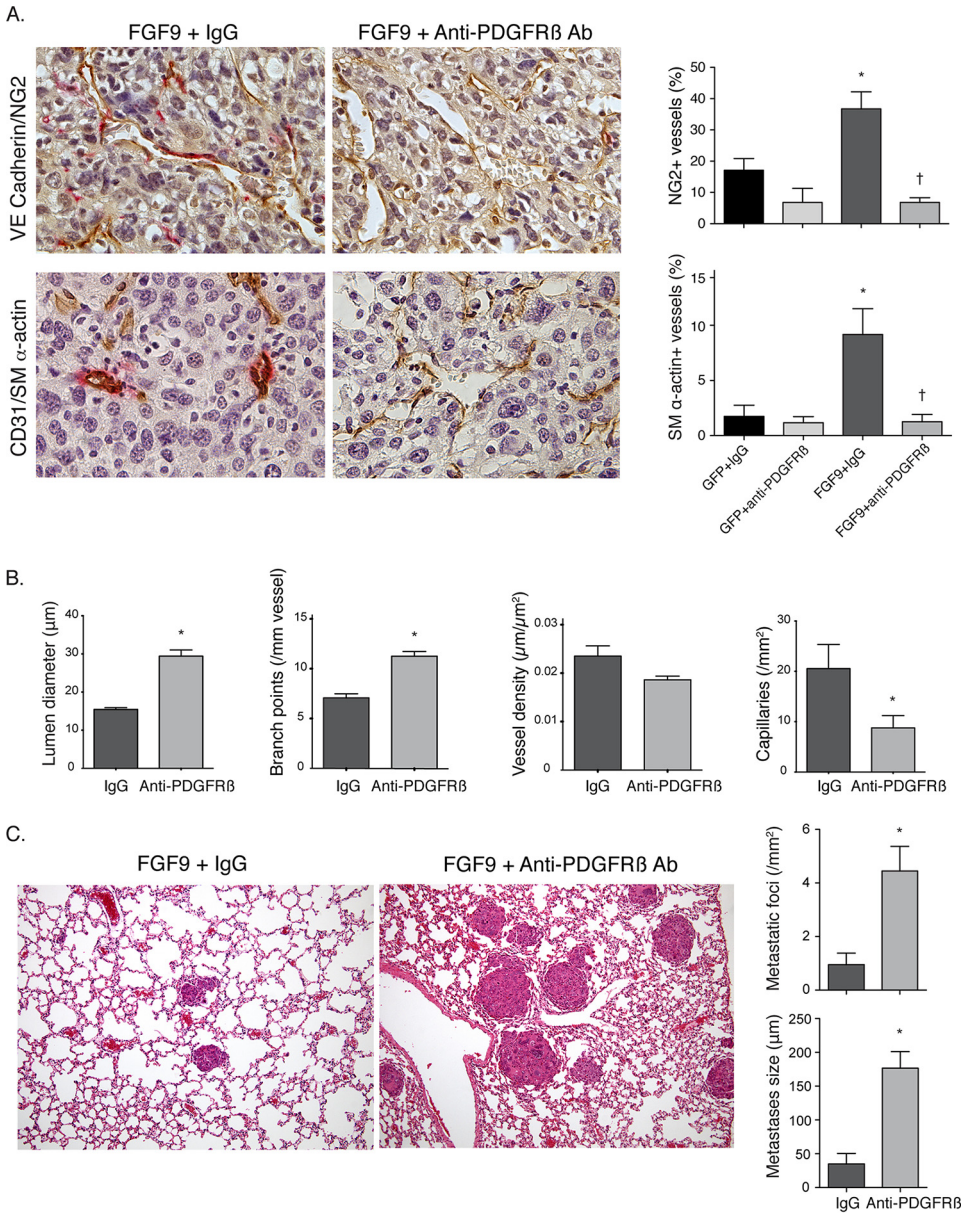

FIGURE 8. **PDGFRβ blockade abrogates the effects of FGF9 on tumor vessels and metastasis.** *A,* micrographs of zinc-fixed renal tumor sections harvested 10 days after orthotopic injection of Renca cell and immunostained for NG2 (*red*) and VE-cadherin (*brown*) or SM α-actin (*red*) and CD31 (*brown*). PDGFRβ-blocking antibody or isotype-matched IgG was applied on day 7. On the *right* are graphs depicting the percentage of microvessels invested with NG2-positive pericytes or SM α-actin-positive mural cells (*top*, *, $p = 0.026$ *versus* GFP + IgG; †, $p = 0.006$ *versus* FGF9 + IgG) (*lower*, *, $p = 0.027$ *versus* GFP + IgG; †, $p = 0.038$ *versus* FGF9 + IgG). *B,* data from FGF9-incubated tumors exposed to anti-PDGFRβ antibody or control IgG, depicting vascular lumen diameter (*, $p < 0.001$), branch point density (*, $p = 0.003$), length density ($p = 0.094$) or capillary density (*, $p = 0.046$). Data are derived from analysis of intravital microscopy videos. *C,* hematoxylin and eosin-sections of lungs, harvested 10 days after orthotopic injection of FGF9-Renca cells with subsequent exposure of primary tumors to anti-PDGFRβ antibody or control IgG. On the *right* are graphs depicting the density and size of intrapulmonary metastases (*, $p = 0.002$; *, $p < 0.001$, respectively).

this region. This is important because a key reason for dysfunctional angiogenesis in tumors is unremitting stimulation by VEGF. The persistent hypoxia leads to sustained VEGF expression, which both drives excessive endothelial sprouting and inhibits mural cell function (36). This yields an aberrant vasculature that cannot reverse the hypoxia (31). The current findings indicate that delivery of FGF9 can effectively break this self-perpetuating and dysfunctional angiogenesis cycle by enforcing a maturation process on the vasculature. That this maturation process was accomplished by stimulating tumor mesenchymal stromal cells, and not by ablation of endothelial cells, constitutes a novel route to vascular modification in tumors. The central paradigm of vascular normalization to date has been to balance the pro-angiogenesis drive in tumors with anti-angiogenesis drugs. Our findings suggest an alternative paradigm, specifically, to balance the innate pro-angiogenic responses in the tumor with pro-maturation responses. Importantly, this paradigm avoids vascular destruction.

We established that PDGFRβ-expressing stromal cells were central to the productive vascular remodeling conferred by FGF9. Previous studies have established that PDGFRβ marks mesenchymal cells, including progenitor populations (43). As

well, FGF9 has been shown to amplify mesenchymal progenitors in developing tissues (19, 30). In the renal tumors, we found that FGF9 amplified PDGFRβ^+ cells, both in the interstitium and also surrounding vessel walls. Most of these latter PDGFRβ^+ mural cells were of pericyte identity. We also observed arrangements of PDGFRβ^+ cells in FGF9-expressing tumors that suggested their migration to the vessel wall. As well, upon isolation from the tumor, PDGFRβ-expressing cells proliferated in response to FGF9, whereas tumor-derived endothelial cells and primary tumor cells did not, supporting the selectivity of FGF9 actions. Moreover, blockade of PDGFRβ in the tumors prevented the productive vascular remodeling by FGF9, led to hyperdilation of the channels, and worsened metastases. Together, these findings establish the existence of an FGF9-sensitive, mesenchymal stromal cell population that can be recruited to stabilize and organize the vasculature. Interestingly, FGF9-sensitive stromal cells have also been identified in a prostate tumor model, with epithelial cell-derived FGF9 driving the signal (44, 45). We found no evidence for endogenously produced FGF9 in the renal tumors, although a low abundance cannot be excluded. Regardless, the collective findings support the importance of FGF9-sensitive stromal cells and harnessing the potential of these cells merits attention.

Delivery of a growth factor to tumors seems counterintuitive. However, the suppression of metastases seen upon FGF9 delivery is consistent with other vessel normalization strategies (12, 13), as is the finding that growth of the primary tumor itself was not impacted (12, 46). At least two potential mechanisms can be considered. First, FGF9-mediated strengthening of the microvessel wall with pericytes, SMCs, and basement membrane could physically block tumor intravasation (47). The presence of fibrillar collagen in the basement membrane is in keeping with more robust mural cell performance and could itself increase both the mechanical strength of the basement membrane and its resistance to its proteolysis, recognizing that enzymes that degrade fibrillar collagen are more restricted than those for degrading other basement membrane constituents (22, 48). The second potential mechanism relates to the improved hypoxia, recognizing that hypoxia is a key driver of aggressive tumor behavior (7, 12) and its suppression through microcirculatory differentiation could dampen the invasive phenotype and/or selection of aggressive clones.

FGF9 displayed vascular-biased activity in the Renca tumor. This bias was based, at least in part, on a relative deficiency of the IIIc "mesenchymal" FGF receptor isoforms on Renca cells. The Renca cells also showed no proliferation, migration, or apoptosis in response to FGF9 and minimal ERK1/2 activation. Because this profile may not be common, caution is required in generalizing the vascular-biased effects of FGF9 to other tumors. Indeed, FGF9 could be deleterious to some tumors (49). The extent to which the current findings with renal tumors will translate to human renal carcinoma is also unknown. It is nonetheless noteworthy that renal cell carcinomas have not been prominently associated with FGF signaling and there is no evidence implicating FGF9 signaling in the initiation or progression of renal tumors (27). Although speculative, profiling tumors for FGF9 receptors and/or tumor cell responsiveness to FGF9 might be a means of gauging the appropriateness of an FGF9-based vascular optimization strategy.

In summary, delivery of FGF9 to aggressive renal tumors in mice produced advanced microvasculature differentiation, with vessel hierarchy and vasoreactivity. The findings suggest a paradigm of harnessing local mesenchymal stromal cells for microcirculatory support. If accomplished selectively, this has the potential to favorably impact tumor behavior.

Author Contributions—H. Y. and M. J. F. contributed to the study design, undertook the tumor characterization, and performed and analyzed cell culture studies. J. M. A. and M. J. F. performed and analyzed the intravital microscopy experiments. Z. N. undertook tumor harvesting, histology, and immunostaining. C. O. undertook Western blot analyses and contributed to the culture and mouse experiments. Y. X. and A. D. W. quantitatively analyzed tumor hypoxia. B. B. performed and analyzed the cell migration studies. S. C. undertook the electron microscopy. C. G. E. contributed to the design and analysis of the intravital microscopy experiments. R. G. undertook and optimized the renal carcinoma model and antibody delivery strategy. J. G. P. conceived and coordinated the study, interpreted the data, and wrote the paper. All authors reviewed the results and approved the final version of this manuscript.

References

1. Folkman, J. (1971) Tumor angiogenesis: therapeutic implications. *N. Engl. J. Med.* **285,** 1182–1186
2. Chung, A. S., Lee, J., and Ferrara, N. (2010) Targeting the tumour vasculature: insights from physiological angiogenesis. *Nat. Rev. Cancer* **10,** 505–514
3. Ebos, J. M., and Kerbel, R. S. (2011) Antiangiogenic therapy: impact on invasion, disease progression, and metastasis. *Nat. Rev. Clin. Oncol.* **8,** 210–221
4. Jain, R. K. (2005) Normalization of tumor vasculature: an emerging concept in antiangiogenic therapy. *Science* **307,** 58–62
5. Nagy, J. A., Chang, S. H., Dvorak, A. M., and Dvorak, H. F. (2009) Why are tumour blood vessels abnormal and why is it important to know? *Br. J. Cancer* **100,** 865–869
6. Fukumura, D., Duda, D. G., Munn, L. L., and Jain, R. K. (2010) Tumor microvasculature and microenvironment: novel insights through intravital imaging in pre-clinical models. *Microcirculation* **17,** 206–225
7. De Bock, K., Mazzone, M., and Carmeliet, P. (2011) Antiangiogenic therapy, hypoxia, and metastasis: risky liaisons, or not? *Nat. Rev. Clin. Oncol.* **8,** 393–404
8. Goel, S., Duda, D. G., Xu, L., Munn, L. L., Boucher, Y., Fukumura, D., and Jain, R. K. (2011) Normalization of the vasculature for treatment of cancer and other diseases. *Physiol. Rev.* **91,** 1071–1121
9. Pàez-Ribes, M., Allen, E., Hudock, J., Takeda, T., Okuyama, H., Viñals, F., Inoue, M., Bergers, G., Hanahan, D., and Casanovas, O. (2009) Antiangiogenic therapy elicits malignant progression of tumors to increased local invasion and distant metastasis. *Cancer Cell* **15,** 220–231
10. Ebos, J. M., Lee, C. R., Cruz-Munoz, W., Bjarnason, G. A., Christensen, J. G., and Kerbel, R. S. (2009) Accelerated metastasis after short-term treatment with a potent inhibitor of tumor angiogenesis. *Cancer Cell* **15,** 232–239
11. Tong, R. T., Boucher, Y., Kozin, S. V., Winkler, F., Hicklin, D. J., and Jain, R. K. (2004) Vascular normalization by vascular endothelial growth factor receptor 2 blockade induces a pressure gradient across the vasculature and improves drug penetration in tumors. *Cancer Res.* **64,** 3731–3736
12. Mazzone, M., Dettori, D., Leite de Oliveira, R., Loges, S., Schmidt, T., Jonckx, B., Tian, Y. M., Lanahan, A. A., Pollard, P., Ruiz de Almodovar, C., De Smet, F., Vinckier, S., Aragonés, J., Debackere, K., Luttun, A., Wyns, S., Jordan, B., Pisacane, A., Gallez, B., Lampugnani, M. G., Dejana, E., Simons, M., Ratcliffe, P., Maxwell, P., and Carmeliet, P. (2009) Heterozygous defi-

ciency of PHD2 restores tumor oxygenation and inhibits metastasis via endothelial normalization. *Cell* **136,** 839–851
13. Maes, H., Kuchnio, A., Peric, A., Moens, S., Nys, K., De Bock, K., Quaegebeur, A., Schoors, S., Georgiadou, M., Wouters, J., Vinckier, S., Vankelecom, H., Garmyn, M., Vion, A. C., Radtke, F., Boulanger, C., Gerhardt, H., Dejana, E., Dewerchin, M., Ghesquière, B., Annaert, W., Agostinis, P., and Carmeliet, P. (2014) Tumor vessel normalization by chloroquine independent of autophagy. *Cancer Cell* **26,** 190–206
14. Jain, R. K. (1988) Determinants of tumor blood flow: a review. *Cancer Res.* **48,** 2641–2658
15. Less, J. R., Skalak, T. C., Sevick, E. M., and Jain, R. K. (1991) Microvascular architecture in a mammary carcinoma: branching patterns and vessel dimensions. *Cancer Res.* **51,** 265–273
16. Baum, O., Vieregge, M., Koch, P., Gül, S., Hahn, S., Huber-Abel, F. A., Pries, A. R., and Hoppeler, H. (2013) Phenotype of capillaries in skeletal muscle of nNOS-knockout mice. *Am. J. Physiol. Regul. Integr. Comp. Physiol.* **304,** R1175–1182
17. Colvin, J. S., White, A. C., Pratt, S. J., and Ornitz, D. M. (2001) Lung hypoplasia and neonatal death in Fgf9-null mice identify this gene as an essential regulator of lung mesenchyme. *Development* **128,** 2095–2106
18. Lavine, K. J., White, A. C., Park, C., Smith, C. S., Choi, K., Long, F., Hui, C. C., and Ornitz, D. M. (2006) Fibroblast growth factor signals regulate a wave of Hedgehog activation that is essential for coronary vascular development. *Genes Dev.* **20,** 1651–1666
19. Geske, M. J., Zhang, X., Patel, K. K., Ornitz, D. M., and Stappenbeck, T. S. (2008) Fgf9 signaling regulates small intestinal elongation and mesenchymal development. *Development* **135,** 2959–2968
20. Lin, Y., Chen, L., Lin, C., Luo, Y., Tsai, R. Y., and Wang, F. (2009) Neuron-derived FGF9 is essential for scaffold formation of Bergmann radial fibers and migration of granule neurons in the cerebellum. *Dev. Biol.* **329,** 44–54
21. Frontini, M. J., Nong, Z., Gros, R., Drangova, M., O'Neil, C., Rahman, M. N., Akawi, O., Yin, H., Ellis, C. G., and Pickering, J. G. (2011) Fibroblast growth factor 9 delivery during angiogenesis produces durable, vasoresponsive microvessels wrapped by smooth muscle cells. *Nat. Biotechnol.* **29,** 421–427
22. Vafaie, F., Yin, H., O'Neil, C., Nong, Z., Watson, A., Arpino, J. M., Chu, M. W., Wayne Holdsworth, D., Gros, R., and Pickering, J. G. (2014) Collagenase-resistant collagen promotes mouse aging and vascular cell senescence. *Aging Cell* **13,** 121–130
23. Salup, R. R., Herberman, R. B., and Wiltrout, R. H. (1985) Role of natural killer activity in development of spontaneous metastases in murine renal cancer. *J. Urol.* **134,** 1236–1241
24. Fera, E., O'Neil, C., Lee, W., Li, S., and Pickering, J. G. (2004) Fibroblast growth factor-2 and remodeled type I collagen control membrane protrusion in human vascular smooth muscle cells: biphasic activation of Rac1. *J. Biol. Chem.* **279,** 35573–35582
25. Yin, H., van der Veer, E., Frontini, M. J., Thibert, V., O'Neil, C., Watson, A., Szasz, P., Chu, M. W., and Pickering, J. G. (2012) Intrinsic directionality of migrating vascular smooth muscle cells is regulated by NAD^+ biosynthesis. *J. Cell Sci.* **125,** 5770–5780
26. Small, T. W., Bolender, Z., Bueno, C., O'Neil, C., Nong, Z., Rushlow, W., Rajakumar, N., Kandel, C., Strong, J., Madrenas, J., and Pickering, J. G. (2006) Wilms' tumor 1-associating protein regulates the proliferation of vascular smooth muscle cells. *Circ. Res.* **99,** 1338–1346
27. Peña-Llopis, S., Vega-Rubín-de-Celis, S., Liao, A., Leng, N., Pavía-Jiménez, A., Wang, S., Yamasaki, T., Zhrebker, L., Sivanand, S., Spence, P., Kinch, L., Hambuch, T., Jain, S., Lotan, Y., Margulis, V., Sagalowsky, A. I., Summerour, P. B., Kabbani, W., Wong, S. W., Grishin, N., Laurent, M., Xie, X. J., Haudenschild, C. D., Ross, M. T., Bentley, D. R., Kapur, P., and Brugarolas, J. (2012) BAP1 loss defines a new class of renal cell carcinoma. *Nat. Genet.* **44,** 751–759
28. Sato, Y., Yoshizato, T., Shiraishi, Y., Maekawa, S., Okuno, Y., Kamura, T., Shimamura, T., Sato-Otsubo, A., Nagae, G., Suzuki, H., Nagata, Y., Yoshida, K., Kon, A., Suzuki, Y., Chiba, K., Tanaka, H., Niida, A., Fujimoto, A., Tsunoda, T., Morikawa, T., Maeda, D., Kume, H., Sugano, S., Fukayama, M., Aburatani, H., Sanada, M., Miyano, S., Homma, Y., and Ogawa, S. (2013) Integrated molecular analysis of clear-cell renal cell carcinoma. *Nat. Genet.* **45,** 860–867
29. Zhang, X., Ibrahimi, O. A., Olsen, S. K., Umemori, H., Mohammadi, M., and Ornitz, D. M. (2006) Receptor specificity of the fibroblast growth factor family: the complete mammalian FGF family. *J. Biol. Chem.* **281,** 15694–15700
30. White, A. C., Xu, J., Yin, Y., Smith, C., Schmid, G., and Ornitz, D. M. (2006) FGF9 and SHH signaling coordinate lung growth and development through regulation of distinct mesenchymal domains. *Development* **133,** 1507–1517
31. Helmlinger, G., Yuan, F., Dellian, M., and Jain, R. K. (1997) Interstitial pH and pO_2 gradients in solid tumors *in vivo*: high-resolution measurements reveal a lack of correlation. *Nat. Med.* **3,** 177–182
32. Gaengel, K., Genové, G., Armulik, A., and Betsholtz, C. (2009) Endothelial-mural cell signaling in vascular development and angiogenesis. *Arterioscler. Thromb. Vasc. Biol.* **29,** 630–638
33. Crisan, M., Yap, S., Casteilla, L., Chen, C. W., Corselli, M., Park, T. S., Andriolo, G., Sun, B., Zheng, B., Zhang, L., Norotte, C., Teng, P. N., Traas, J., Schugar, R., Deasy, B. M., Badylak, S., Buhring, H. J., Giacobino, J. P., Lazzari, L., Huard, J., and Péault, B. (2008) A perivascular origin for mesenchymal stem cells in multiple human organs. *Cell Stem Cell* **3,** 301–313
34. Kim, K. J., Li, B., Winer, J., Armanini, M., Gillett, N., Phillips, H. S., and Ferrara, N. (1993) Inhibition of vascular endothelial growth factor-induced angiogenesis suppresses tumour growth *in vivo*. *Nature* **362,** 841–844
35. Yuan, F., Chen, Y., Dellian, M., Safabakhsh, N., Ferrara, N., and Jain, R. K. (1996) Time-dependent vascular regression and permeability changes in established human tumor xenografts induced by an anti-vascular endothelial growth factor/vascular permeability factor antibody. *Proc. Natl. Acad. Sci. U.S.A.* **93,** 14765–14770
36. Greenberg, J. I., Shields, D. J., Barillas, S. G., Acevedo, L. M., Murphy, E., Huang, J., Scheppke, L., Stockmann, C., Johnson, R. S., Angle, N., and Cheresh, D. A. (2008) A role for VEGF as a negative regulator of pericyte function and vessel maturation. *Nature* **456,** 809–813
37. Carmeliet, P., and Jain, R. K. (2011) Molecular mechanisms and clinical applications of angiogenesis. *Nature* **473,** 298–307
38. Emblem, K. E., Mouridsen, K., Bjornerud, A., Farrar, C. T., Jennings, D., Borra, R. J., Wen, P. Y., Ivy, P., Batchelor, T. T., Rosen, B. R., Jain, R. K., and Sorensen, A. G. (2013) Vessel architectural imaging identifies cancer patient responders to anti-angiogenic therapy. *Nat. Med.* **19,** 1178–1183
39. Chauhan, V. P., Stylianopoulos, T., Martin, J. D., Popović, Z., Chen, O., Kamoun, W. S., Bawendi, M. G., Fukumura, D., and Jain, R. K. (2012) Normalization of tumour blood vessels improves the delivery of nanomedicines in a size-dependent manner. *Nat. Nanotechnol.* **7,** 383–388
40. Wang, Q., Kocaoglu, O. P., Cense, B., Bruestle, J., Jonnal, R. S., Gao, W., and Miller, D. T. (2011) Imaging retinal capillaries using ultrahigh-resolution optical coherence tomography and adaptive optics. *Invest. Ophthalmol. Vis. Sci.* **52,** 6292–6299
41. Segal, S. S. (2005) Regulation of blood flow in the microcirculation. *Microcirculation* **12,** 33–45
42. Clifford, P. S. (2011) Local control of blood flow. *Adv. Physiol. Educ.* **35,** 5–15
43. Andrae, J., Gallini, R., and Betsholtz, C. (2008) Role of platelet-derived growth factors in physiology and medicine. *Genes Dev.* **22,** 1276–1312
44. Wu, X., Jin, C., Wang, F., Yu, C., and McKeehan, W. L. (2003) Stromal cell heterogeneity in fibroblast growth factor-mediated stromal-epithelial cell cross-talk in premalignant prostate tumors. *Cancer Res.* **63,** 4936–4944
45. Jin, C., Wang, F., Wu, X., Yu, C., Luo, Y., and McKeehan, W. L. (2004) Directionally specific paracrine communication mediated by epithelial FGF9 to stromal FGFR3 in two-compartment premalignant prostate tumors. *Cancer Res.* **64,** 4555–4562
46. Agrawal, V., Maharjan, S., Kim, K., Kim, N. J., Son, J., Lee, K., Choi, H. J., Rho, S. S., Ahn, S., Won, M. H., Ha, S. J., Koh, G. Y., Kim, Y. M., Suh, Y. G., and Kwon, Y. G. (2014) Direct endothelial junction restoration results in significant tumor vascular normalization and metastasis inhibition in mice. *Oncotarget* **5,** 2761–2777
47. Xian, X., Håkansson, J., Ståhlberg, A., Lindblom, P., Betsholtz, C., Ger-

hardt, H., and Semb, H. (2006) Pericytes limit tumor cell metastasis. *J. Clin. Invest.* **116,** 642–651

48. Pickering, J. G., Ford, C. M., Tang, B., and Chow, L. H. (1997) Coordinated effects of fibroblast growth factor-2 on expression of fibrillar collagens, matrix metalloproteinases, and tissue inhibitors of matrix metalloproteinases by human vascular smooth muscle cells. Evidence for repressed collagen production and activated degradative capacity. *Arterioscler. Thromb. Vasc. Biol.* **17,** 475–482
49. Yin, Y., Betsuyaku, T., Garbow, J. R., Miao, J., Govindan, R., and Ornitz, D. M. (2013) Rapid induction of lung adenocarcinoma by fibroblast growth factor 9 signaling through FGF receptor 3. *Cancer Res.* **73,** 5730–5741